Characterization and Application of Nanomaterials 2025, 8(2), 10461.
https://doi.org/10.24294/can10461

Article

Insight into zero-valent iron at the nanoscale and its silica composites: Synthesis and characterization

Elsayed El-Mossalamy[1,*], Ahmed Al-Owais[2], Ibrahim El-Hallag[3]

[1] Chemistry Department, Faculty of Science, Benha University, Benha 13511, Egypt
[2] Chemistry Department, College of Science, King Saud University, Riyadh 11451, Saudi Arabia
[3] Chemistry Department, Faculty of Science, Tanta University, Tanta 31527, Egypt
*** Corresponding author:** Elsayed El-Mossalamy, alsayed.almosallamy@fsc.bu.edu.eg

CITATION

El-Mossalamy E, Al-Owais A, El-Hallag I. Insight into zero-valent iron at the nanoscale and its silica composites: Synthesis and characterization. Characterization and Application of Nanomaterials. 2025; 8(2): 10461. https://doi.org/10.24294/can10461

ARTICLE INFO

Received: 21 November 2024
Accepted: 31 December 2024
Available online: 2 April 2025

Abstract: Nanoscale zero-valent iron (nZVI) is thought to be the most effective remediation material for contaminated soil, especially when it comes to heavy metal pollutants. In the current high-industrial and technologically advanced period, water pollution has emerged as one of the most significant causes for concern. In this instance, silica was coated with zero-valent iron nanoparticles at 650 and 800 °C. Ferric iron with various counter-ions, nitrate (FN) and chloride (FC), and sodium borohydride as a reducing agent were used to create nanoscale zero-valent iron in an ethanol medium with nitrogen ambient conditions. X-ray diffraction (XRD) and field emission scanning electron microscopy (FE-SEM) techniques were employed to describe the structures of the generated zero-valent iron nanoparticles. Further, we investigated the electrical properties and adsorption characteristics of dyes such as alizarin red in an aqueous medium. As a result, zero-valent nano iron (nZVI), a core-shell environmental functional material, has found extensive application in environmental cleanup. The knowledge in this work will be useful for nZVI-related future research and real-world applications.

Keywords: nanoscale; nZVI; ferric nitrate; ferric chloride; alizarin

1. Introduction

Because of their unique properties that distinguish them from bulk materials, nanoscale materials have garnered a lot of attention recently. It's interesting to note that zerovalent metal nanostructures, such as Galdames et al. [1]; Krebsz and Pasinszki [2]; Pereira et al. [3]; and Petrarca et al. [4], or their related composites, may find use in research and technology. Among the many possible applications for metallic nanostructures are biomedicine [4], environmental remediation [5], energy storage and harvesting, and catalysis [6]. This is a result of their exceptional physical characteristics. For uses in computer technology, bioimaging, electronics, optics, photonics, data storage, and high-frequency applications.

It is crucial to keep in mind that the conditions and techniques employed during synthesis have a significant impact on the final materials' structure, dielectric characteristics, and magnetic characteristics [7]. Farzana et al. [8] used hydrothermal preparation at various reaction temperatures to create a range of cobalt ferrite nanoparticles. They discovered that the sample with the highest saturation magnetisation, 150.67 emu/g, was the one made at the highest temperature. The dielectric characteristics, however, are unaffected by the synthesis temperature. At the nanoscale, metallic particles can be created essentially in two ways: "top-down" and "bottom-up". Bulk metal grinding serves as an example of how top-down approaches struggle with narrow particle size distributions [9]. Conversely, bottom-up methods offer a precise, suitable distribution of particle sizes.

Atomic or molecular precursors in the gas or solution phase serve as the starting point for this process, which builds up nuclei that gradually increase until they form nanoparticles. Temperature, the type of stabilizing agent, and concentrations are kinetic characteristics that affect the nanoparticle's ability to form various structures, shapes, and sizes. Precipitation methods have been used to create manufactured nanoparticles (MNPs) for zero-valent iron throughout the past few decades [10]. The following reaction Equation (1) [11] illustrates the most popular technique for environmental reasons: The reduction of Fe (II) or Fe (III) cation solutions using borohydride anion.

$$2\mathrm{FeCl_3} + 6\mathrm{NaBH_4} + 18\mathrm{H_2O} \rightarrow 2\mathrm{Fe^0} + 6\mathrm{NaCl} + 6\mathrm{B(OH)_3} + 21\mathrm{H_2} \qquad (1)$$

Maintaining iron in its zerovalent forms requires a range of aqueous media types. Zero-valent iron makes up the majority of the ore, whereas mixed oxides such as F_3O_4, Fe_2O_3, and FeOOH make up the shell of the nZVI particle [12]. As a result of its effective electron donation, this type of metallic iron forms a mixed oxide/hydroxide shell that influences the bulk composition, surface charge, and morphologies of nZVI. Consequently, surface oxidation, aggregation propensity, magnetic characteristics, and environmental interactions were affected. The iron metal can react with oxygen carriers in a variety of ways, oxidising to produce a sub-oxide shell. It is expected that this oxidation reaction will generate a very high rate of heat, particularly for the ultra-small particle [13]. Numerous investigations have been carried out on the oxidation of metallic nanoparticles, the oxidation of bulk iron by oxygen and water vapour [14,15], and the oxidation of metal films at low temperatures when exposed to oxygen gas [16,17].

Three steps were involved in the oxidation of iron nanoparticles: Fe_3O_4 partially oxidised into the α-Fe_2O_3 structure, Fe_3O_4 and iron core fully oxidised into the α-Fe_2O_3 phase, and then the iron core oxidised into crystalline iron oxides and disordered phase formation. The size, shape, and morphologies of iron metal nanoparticles have been shown to affect the degree of heat sensitivity. It is essential to comprehend the high-temperature oxidation processes that include various nanoscale particle sizes. Additionally, ZVI (zero valent iron) materials are used in a wide range of sectors, particularly in soil and groundwater remediation, such as the removal of heavy metals, organophosphates, dyes, antibiotics, and other organic pollutants [18–22].

The synthesis of nZVI under aqueous circumstances has been the subject of numerous research articles in recent years. However, not enough research has been done on how iron nanoparticles are produced in ethanol. In order to avoid severe oxidation, the objective of this endeavour is to synthesise nZVI outdoors using ethanol while simultaneously describing the materials' size and surface characteristics [11]. In this study, we synthesised and investigated iron-based nanoparticles in the zero-oxidation condition. The materials were described by means of XRD, FE-SEM, electrical conductivity, real and imaginary components of the dielectric constant, and the loss tangent (tan δ) approach. Furthermore, it was assessed if nZVIs derived from different precursors could adsorb a model dye such as Alizarin red.

2. Experimental

2.1. Materials

Alizarin red dye [sodium alizarin sulphonate ($C_{14}H_7NaO_7S$), ferric nitrate [$Fe(NO_3)3.9H_2O$], sodium borohydride ($NaBH_4$), and ferric chloride anhydrous ($FeCl_3$) were supplied by Sigma-Aldrich Chemical Company. All of these materials were employed without additional refinement. Aluminium foils, aluminium scrapes, and plates with 98% sodium hydroxide were employed, along with commercial sodium silicate solution with a solid concentration of 45%. The other reagents were all analytical reagent grade, and deionized water was used. **Figure 1** depicts the chemical structure of alizarin red dye.

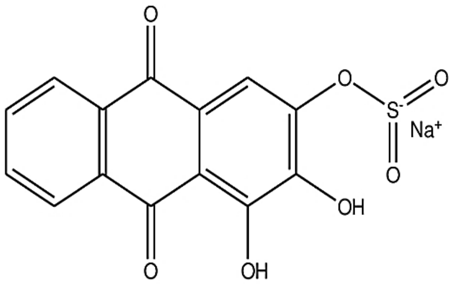

Figure 1. Alizarin red dye's chemical structure.

2.2. Method

The creation of nanoscale zero-valent iron (nZVIs) from various counter-ions impregnated with silica is the focus of this work. It was used as an adsorbent to remove the alizarin red dye from aqueous media. **Figure 2** shows how to produce of the iron nanoparticles by reduction with sodium borohydride ($NaBH_4$) in a flask reactor in an ethanol medium with three open necks. The following is the reaction:

$$2FeX_n + 6NaBH_4 + 18H_{2O} \rightarrow 2Fe^0 + 6NaX + 6B(OH)_3 + 21H_2 \quad (2)$$

where X = Cl^- and NO_3^-.

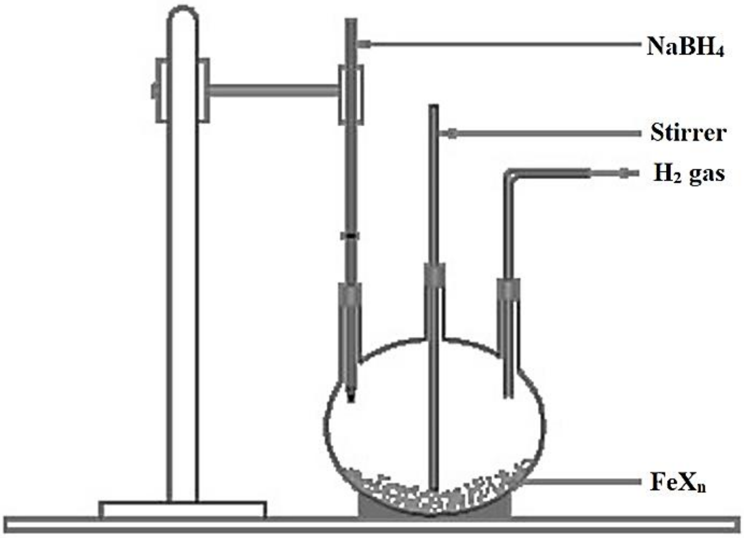

Figure 2. Schematic diagram for the synthesis of iron and its composite nanoparticles.

2.2.1. Preparation of nZVI particles

For the synthesis of nanoscale zero-valent iron **(**nZVIs) (A and B), where A is (Fe^0/Cl^-)] and B is (Fe^0/NO_3^-) from different anions such as chloride (Cl^-) and nitrate (NO_3^-), a 0.6 M solution of each salt was dissolved in a 4/1 (v/v) ethanol/water mixture (24 ml ethanol + 6 ml deionized water) and stirred well. However, a 0.8 M sodium borohydride solution was made, which is equivalent to dissolving 3.028 g of $NaBH_4$ in 100 ml of deionized water. This is because promoting the synthesis of iron nanoparticles requires a greater amount of borohydride. Poured into a burette, the borohydride solution is added drop by drop—one drop every two seconds—to each solution while being vigorously stirred. As soon as the first drop of sodium borohydride solution was added, black solid particles appeared. To speed up the reduction reaction, the remaining sodium borohydride was subsequently added drop by drop. The entire borohydride solution was added to the mixture and stirred for a further thirty minutes. The liquid phase was separated from the black iron nanoparticles using the vacuum filtration process. In order to eliminate all of the water, the solid particles were thoroughly cleaned three times using 25 ml parts of 100% ethanol. The washing process is perhaps the most crucial step in the synthesis process because it prevents the rapid oxidation of zero-valent iron nanoparticles.

Last but not least, the produced nanoparticles were dried for an entire night at 60 °C. To prevent the nano iron particles from oxidizing, a thin layer of ethanol was applied before storage.

2.2.2. Preparation of SiO_2 nanoparticles

SiO_2 nanoparticles were created using a sol-gel auto-combustion process with two distinct fuels—fructose and glucose. Fuels were used as the reductant precursor and nitric acids as the oxidant precursor to create SiO_2 nanoparticles. Sg and S_f, respectively, are the SiO_2 samples that are made utilizing glucose and fructose as fuels. The total oxidising and reducing valences of the fuel and oxidiser are used to determine the stoichiometric compositions of the redox mixtures for combustion. This ensures that the energy released during combustion is maximized for each reaction by ensuring that the equivalency ratio, ϕc, is unity (i.e., ϕc = 1) [23]. 6 g of silica gel were dissolved by swirling in a hot (50 ml, 4 M) solution in a standard synthesis procedure. NaOH. 50 ml of 4M HNO_3 was subsequently added to the created solution dropwise, resulting in a colourless gel. The surplus sodium hydroxide was eliminated from the generated gel by thoroughly washing it multiple times with diluted HNO_3. Using 0.1 M HNO_3, the mixture's pH was brought to 8. Heat the reaction with an aqueous hot solution (20 ml) containing (3.963 g, 0.02 mol glucose or 3.603 g, 0.02 mol fructose) to 80 ℃ and stir for an hour. As the mixture heated to 120 ℃, it gelled. After the gel was created, it was burnt on a hot plate at 350 ℃ to produce a dry, gray mass. This mass was then calcined for four hours at 800 ℃ in an electric furnace to produce samples Sg and Sf, respectively.

2.2.3. Impregnation of nZVI with silica

The nZVI carrier was silicon. The process of creating the nZVI using silica involved two steps: F is Fe^0/NO_3^- impregnated with S_f, and Fe is Fe^0/Cl^- impregnated with Sg. Initially, ferric salts, like ferric chloride or ferric nitrate, were adsorbed or wet-impregnated onto silica. Then, loaded iron was reduced by $NaBH_4$ to Fe^0 [24]. In the adsorption process, 20 mL of a ferric salt solution—such as ferric chloride or ferric nitrate solution—containing 1 mol/L was mixed with 2 g of silica. A rotary shaker set at 25 ℃ was used to shake the mixture for 24 h. After that, the mixture was mixed with 15 mL of ethanol and 15 mL of water. Subsequently, 50 mL of 1 mol/L $NaBH_4$ was added to the mixture while vigorously swirling and dropping the liquid. Ultimately, the produced nanoparticles were dried for an entire night at 60 ℃ in an oven.

2.3. Characterization methods

The generated products were measured by X-ray powder diffraction using an 18 KW diffractometer (Bruker; model D8 advance) with monochromatic Cu-Ka radiation, 1.54178 (Å). X-ray diffraction was used to evaluate the as-prepared nanomaterials for crystallinity and phase purity. With a step size of 0.02° (2 θ) and a scan step length of 0.4 s, the diffraction patterns were rearranged at room temperature within the angular range of 30°–90° (2 θ).

With an accelerating voltage of 20 KV, a field emission scanning electron microscope (FE-SEM, JEOL JSM-6510LV) was used to examine the morphology and elemental content of the as-prepared nanomaterials.

The frequency range used for the AC measurements was 500 Hz to 5 MHz. Using a programmed automatic RCL meter (HIOK3532LCR HITESTER), the values of impedance (Z), capacitance (C), resistance (R), and phase angle (υ) can be immediately read.

The real part of the dielectric constant, έ , the imaginary part, ε″ , and the dielectric loss tangent, tan δ, were calculated using the data of Z, C, R, and ϕ at any frequency F. **Figure 3** depicts the sample holder that was utilized for the AC measurements.

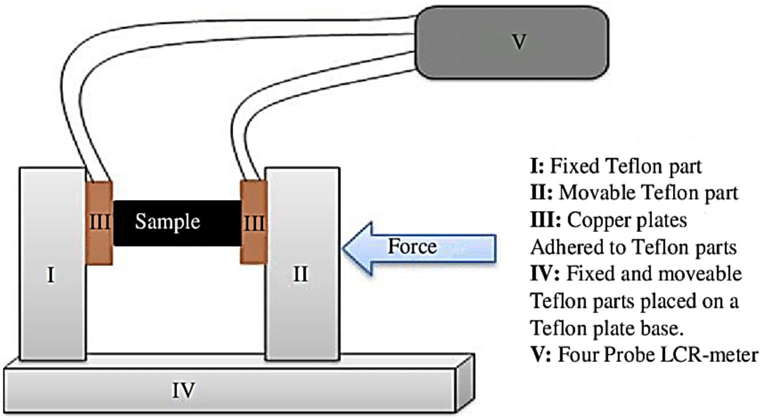

Figure 3. The sample holder was used for AC measurement.

3. Results and discussion

3.1. X-ray diffraction study

Figure 4a,**b** illustrate the XRD analysis of FC and FN nanoparticles, respectively, in the characterization of produced nZVI particles. When α-Fe^0 nanoparticles are present in the sample for FC and FN nanoparticles, the peaks at 2θ 44.87° and 44.68°, respectively, show 100% intensity. It was discovered that the average crystalline diameters of the FC and FN nanoparticles were 3.166 and 1.83 nm, respectively.

The peaks at 2 θ 44.87° and 44.68°, respectively, indicate the existence of iron nanoparticles (Fe^0). Particle size can be presumed with the XRD by using the Scherer equation [25]:

$$D = \frac{0.9\lambda}{\beta \cos\theta} \tag{3}$$

where θ is the Bragg angle derived from 2 θ, which corresponds to the greatest peak intensity, β is the full width at half maximum (FWHM), D is the particle size (in nanometres), and λ is the wavelength of the Cu Kα radiation, which is 0.154 nm [26,27]. Accordingly, the crystalline particle size was found to be 50 nm and 59 nm, respectively.

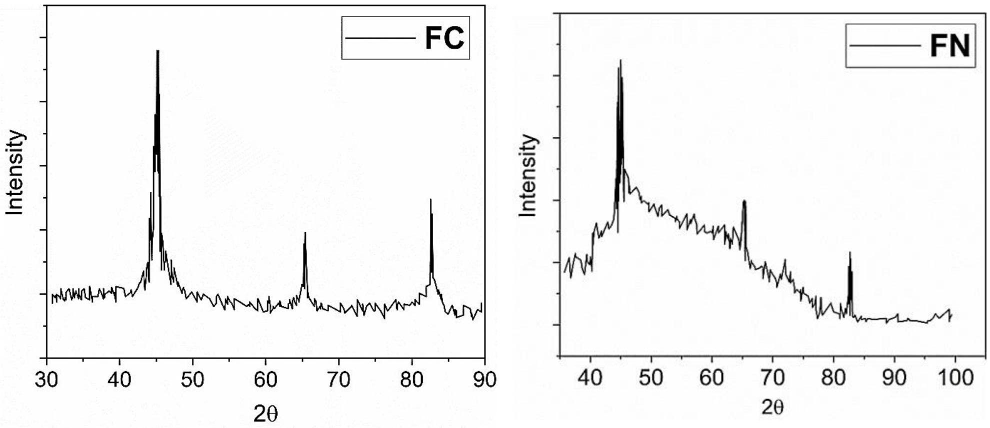

(**a**) (**b**)

Figure 4. (**a**) X-ray diffraction (XRD) pattern of FC and (**b**) FN.

3.2. FE-SEM

Particle size and morphology of the produced nZVI (FC and FN samples) were examined at different magnifications using an FE-SEM (**Figure 5**). FE-SEM pictures of produced nZVI nanoparticles are displayed in **Figure 5a–d**. The photos show the presence of crystalline, ultrafine, spherical shapes with aggregation. Aggregation of iron nanoparticles is thought to be caused by the large surface area of the individual particles and the magnetic dipole-dipole interactions. The average particle size of the nZVI nanoparticles (FC sample) was determined using FE-SEM images, and it was discovered to be between 50 and 100 nm. Given that the measured size is greater than the size inferred from the XRD pattern, densification is likely the cause of the appearance of the small particles colliding with one another. Furthermore, FE-SEM images (**Figure 5e–h**) show the morphologies of crystalline spherical networks for FN, with average particle sizes between 50 and 63 nm.

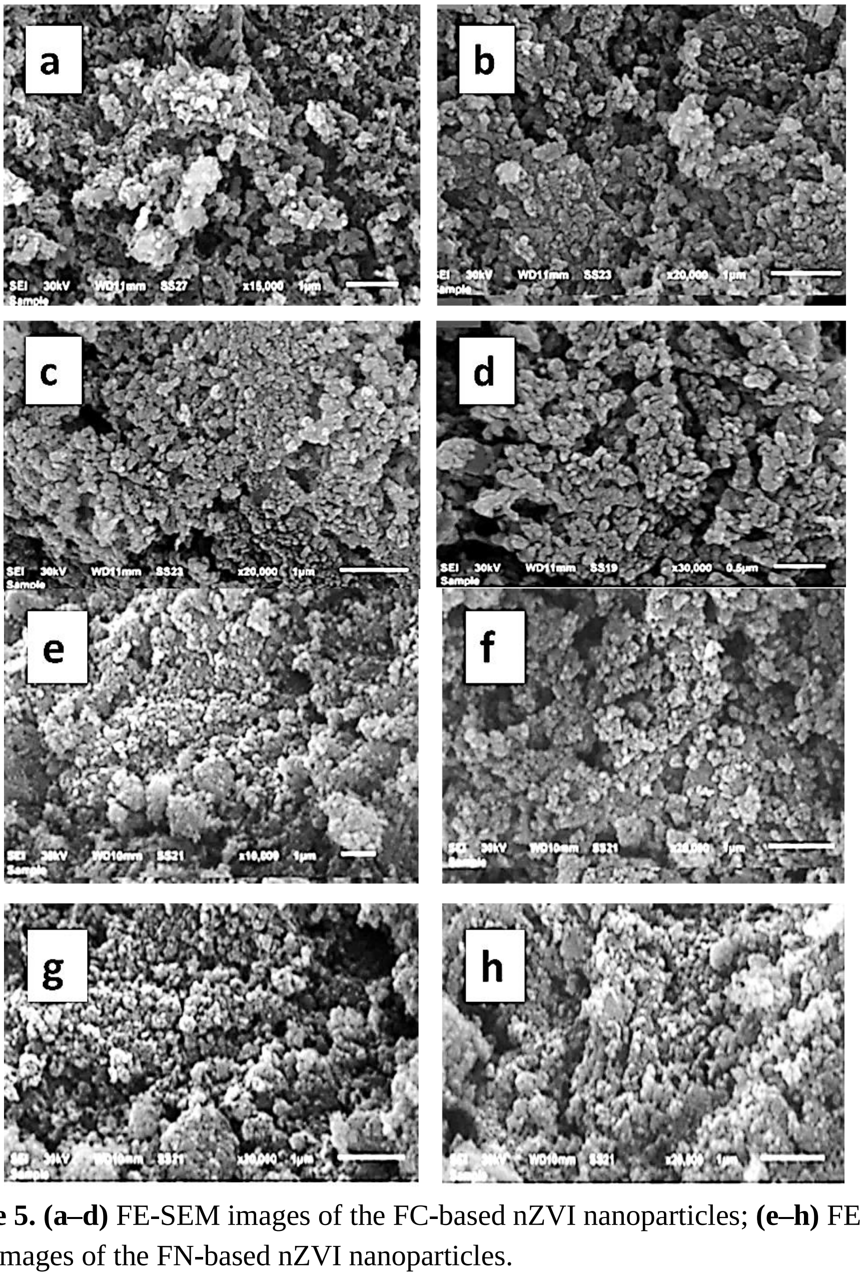

Figure 5. (a–d) FE-SEM images of the FC-based nZVI nanoparticles; **(e–h)** FE-SEM images of the FN-based nZVI nanoparticles.

3.3. Dielectric properties

This article measured, examined, and described the electrical characteristics of different compositions of nZVI as a function of frequency. Two basic electrical properties of nZVI materials are defined with the help of dielectric analysis. Its two main characteristics are its capacitive insulating nature, which indicates its capacity to retain electrical charge, and its conduction nature, which demonstrates its electrical charge transmission capability. The dielectric characteristics of ferric chloride (FC), ferric nitrate (FN), impregnated zero-valent iron prepared from ferric chloride with silica that calcined at 650 ℃ (FCS650), impregnated zero-valent iron prepared from ferric nitrate with silica that calcined at 650 ℃ (FNS650), impregnated zero-valent iron prepared from ferric chloride with silica that calcined at 800 ℃ (FCS800), and impregnated zero-valent iron prepared from ferric chloride with silica that calcined at 800 ℃ (FNS800) of nZVI in the frequency range of 500 Hz to 7 MHz.

As a general aspect of the obtained results, the frequency and composition dependency of the dielectric constant's imaginary (ε") and real (ε') components are examined and explained. As seen in **Figure 6a–c**, the real and imaginary dielectric constants for nanoscale zero-valent iron (nZVI) compositions for FC, FN, FCS800, FNS800, FCS650 and FNS650 fluctuate with frequency (f). For every composition, it can be seen that when frequency increases at room temperature, the real part of the dielectric constants (ε') and the imaginary part of the dielectric constant (ε") both drop in value.

At low frequencies, the values of ε' and ε" reach a maximum value; at higher frequencies, they become frequency dependent, finally reaching a virtually constant value. In the cases of FC and FN, **Table 1** provides the values of the real part (ε') and the imaginary part (ε") of the dielectric constant at a chosen range of frequencies. As frequency increases, it was discovered that the values of ε' decrease. This is because, for polar material, ε' at low frequencies is explained by the combined effects of polarizability, deformational (ionic and electronic), and relaxational (orientational and interfacial) polarization [27].

Initially, valence electron displacement with respect to the positive nucleus is the source of electronic polarization. At frequencies as high as 1016 Hz, this kind of polarization occurs. Positive and negative ions are displaced relative to one another, resulting in ionic polarization, which is the second kind. Third, dipolar polarization happens when a material has molecules with a permanent electric dipole moment that are able to modify their orientation relative to the applied electric field. Dipolar polarization arises at frequencies as high as 1010 Hz. Space charge polarization is the last one, which is brought on by interfaces that impede mobile charge carriers. 1 to 103 Hz is the usual frequency range where space charge polarization happens.

Total polarization for dielectric materials is the sum of the four polarization types mentioned above [28,29]. The current study's acquired results demonstrate that the ionic polarization has little effect on the overall polarization. As a result of taking longer than ionic and electronic polarization, orientational polarization diminishes with increasing frequency. As a result, at higher frequencies, which correspond to interfacial polarization, the value of ε drops and approaches a nearly constant value.

Furthermore, the real dielectric constant (ε') and imaginary dielectric constant (ε'') characteristics at high frequencies for a particular sample indicate that the sample has better optical quality and fewer defects; this parameter is crucial for different nonlinear optical materials and their applications [30].

Figure 6a and **Table 1** show how ε' and ε'' vary in frequency for FC and FN compositions. It is also observed in **Figure 6a–c** that the values of ε' and ε'' vary with the composition of nZVI. This is explained by the expectation that altering the composition of nZVI will modify the structure of the nanoscale zero-valent iron host, resulting in a change in the density of charge defect states and, ultimately, dielectric properties [30].

Table 1. The values of the dielectric constants' real (ε') and imaginary (ε'') parts for FC and FN at a chosen range of frequencies (f).

FC			**FN**		
log f	**log ε'**	**log ε''**	**log f**	**log ε'**	**log ε''**
2	8.517141	10.29946	2	6.0634	7.028084
2.30103	8.168969	9.898106	2.30103	5.837691	6.866628
2.477121	7.996137	9.559789	2.477121	5.684614	6.731304
2.60206	7.861884	9.412483	2.60206	5.566078	6.614058
2.69897	7.752451	9.286082	2.69897	5.467662	6.511132
2.778151	7.661404	9.183051	2.778151	5.38337	6.419377
2.845098	7.586409	9.100253	2.845098	5.30951	6.336554
2.90309	7.519962	9.02646	2.90309	5.245341	6.26439
2.954243	7.461461	8.962467	2.954243	5.187464	6.197963
3	7.408675	8.906876	3	5.134203	6.135486
3.30103	7.068762	8.526559	3.30103	4.783538	5.71765
3.477121	6.865173	8.294816	3.477121	4.575465	5.465311
3.60206	6.721027	8.131624	3.60206	4.435062	5.300488
3.69897	6.607467	8.002585	3.69897	4.321597	5.162792
3.778151	6.491816	7.985738	3.778151	4.225777	5.043593
3.845098	6.408754	7.880472	3.845098	4.146264	4.945795
3.90309	6.340503	7.803268	3.90309	4.077407	4.860372
3.954243	6.279319	7.733654	3.954243	4.018498	4.790034
4	6.22234	7.669767	4	3.961002	4.716288
4.30103	5.846071	7.211311	4.30103	3.587046	4.234645
4.477121	5.624173	6.942541	4.477121	3.36456	3.939705
4.60206	5.467767	6.75456	4.60206	3.21189	3.737767
4.69897	5.343517	6.608181	4.69897	3.088393	3.566371
4.778151	5.248755	6.492814	4.778151	2.994286	3.439241
4.845098	5.169851	6.39393	4.845098	2.915626	3.331743
4.90309	5.100702	6.306038	4.90309	2.84939	3.241104
4.954243	5.045411	6.244957	4.954243	2.791734	3.161801
5	4.993901	6.181048	5	2.741091	3.091871

Table 1. (*Continued*).

FC			**FN**		
log f	**log ε'**	**log ε"**	**log f**	**log ε'**	**log ε"**
5.30103	4.686685	5.847292	5.30103	2.440615	2.67782
5.477121	4.534939	5.706617	5.477121	2.287085	2.466494
5.60206	4.438793	5.626987	5.60206	2.187863	2.331016
5.69897	4.370959	5.587526	5.69897	2.116544	2.235103
5.778151	4.340539	5.375195	5.778151	2.061252	2.161343
5.845098	4.307531	5.377124	5.845098	2.0163	2.102435
5.90309	4.282338	5.37698	5.90309	1.979197	2.054243
5.954243	4.266863	5.383636	5.954243	1.947821	2.014583
6	4.256274	5.403648	6	1.920216	1.979585
6.30103	4.476008	6.100774	6.30103	1.757499	1.785652
			6.477121	1.677107	1.706453
			6.60206	1.62716	1.922624
			6.69897	1.574856	1.898534

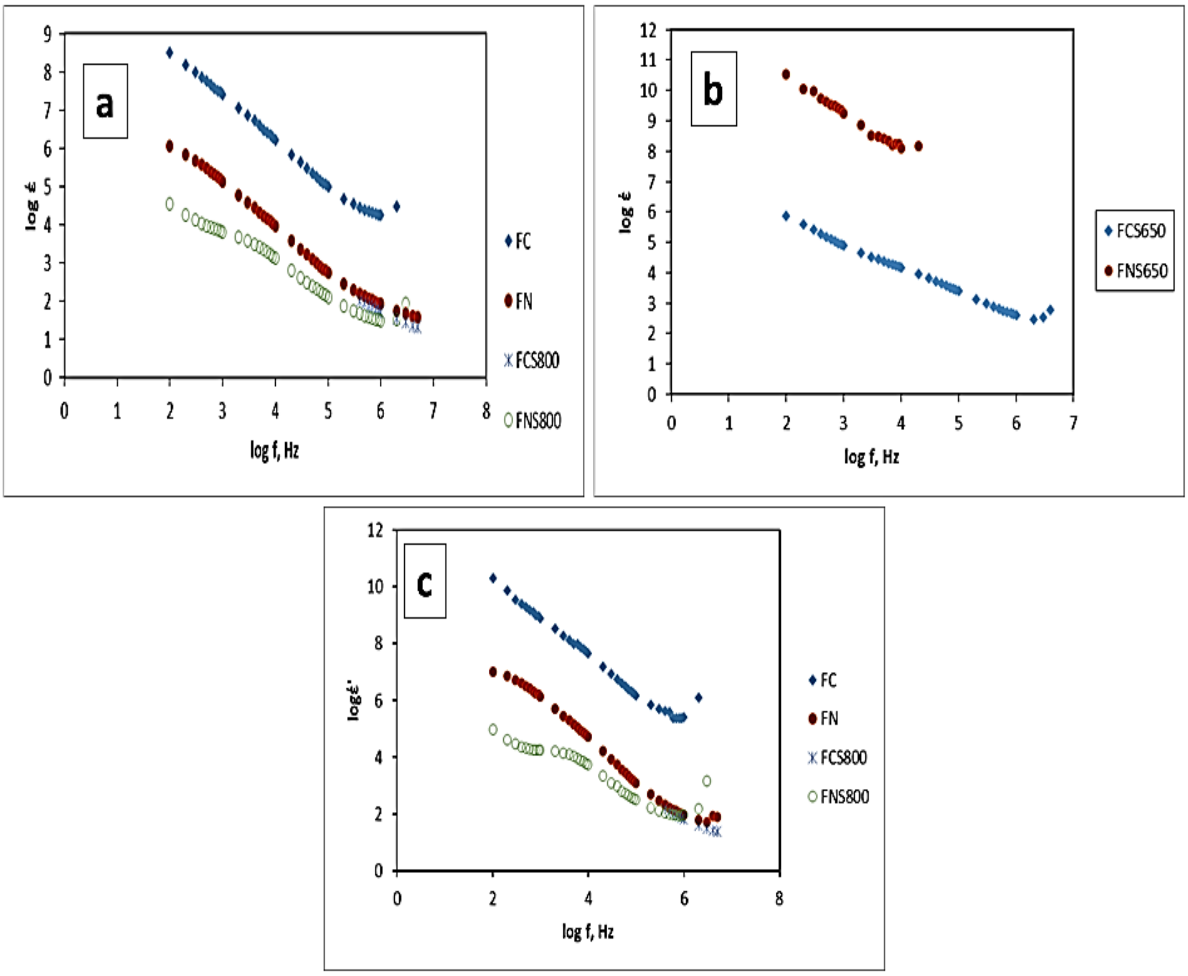

Figure 6. The variation of the real part of the dielectric constant (ε') and the imaginary part of the dielectric constant (ε") with frequencies (f) in the case of **(a)** FC, FN, FCS800, and FNS800; **(b)** FCS650, and FNS650; and **(c)** FC, FN, FCS800, and FNS800.

For the two prepared samples, FC and FN, with nZVI compositions, **Figure 7a** displays the frequency dependence of the dielectric loss tangent (tan (*δ*)). Similar trends to those seen for ε'' at low frequencies can be seen in the variation of tan (*δ*) with frequency at constant temperature. This could be because, up until a frequency of 10, the polarizability contribution from ionic and orientation sources decreases; after that, the dielectric loss tangent tan (*δ*) increases because of their inertia effect [31].

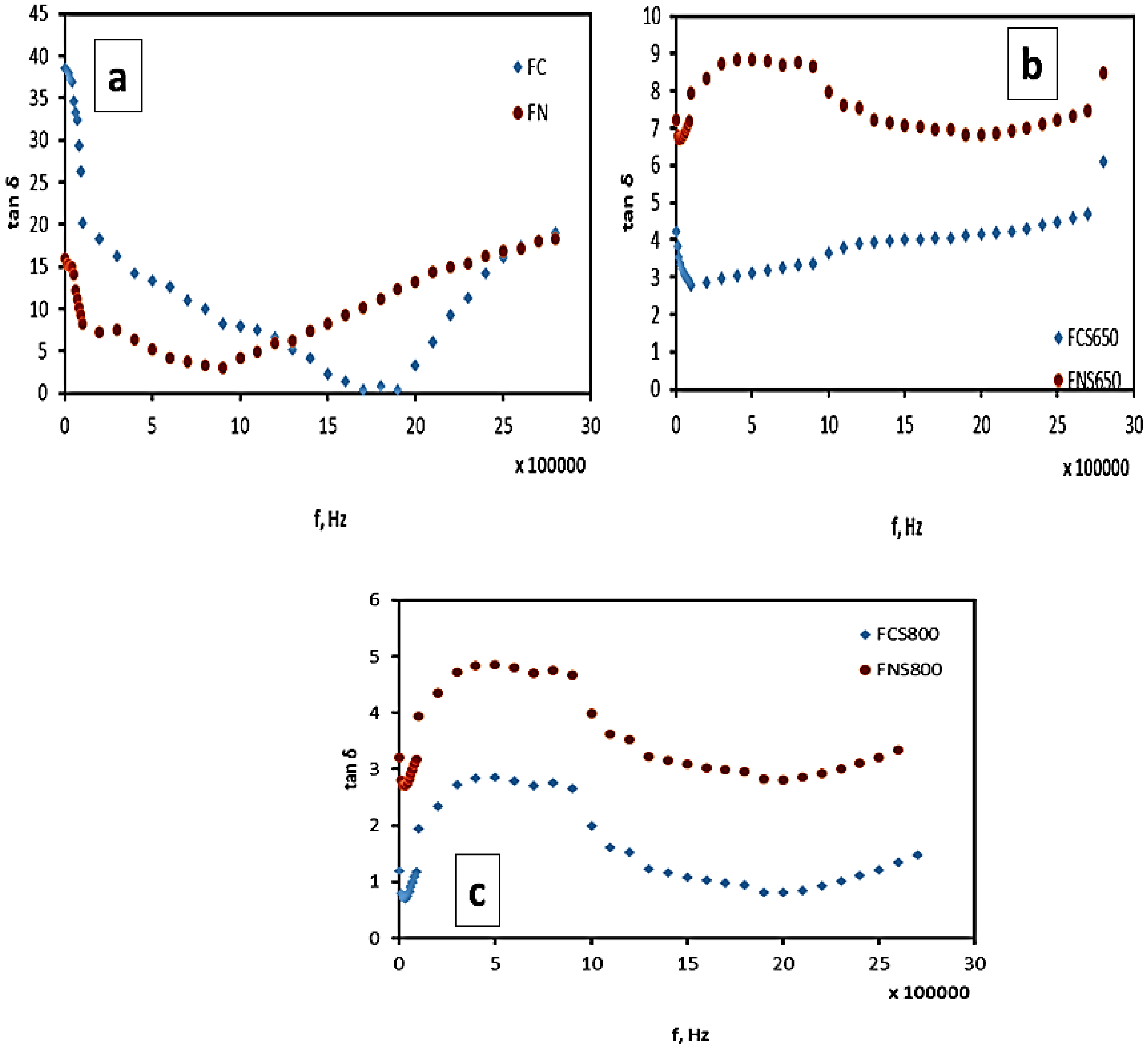

Figure 7. The variation of loss tangent (tan δ) with frequency (f) for **(a)** FC, FN; **(b)** FCS650, FNS650; and **(c)** FCS800, FNS800 for nZVIs.

The loss tangent's fluctuation with frequency for various nZVI compositions is depicted in **Figure 7b,c**. Ionic conduction via nZVI segmental motion is represented by the fingerprint of the single relaxation peak's [32]. The initial increase in the loss tangent at a lower frequency area can be ascribed to the ohmic (active) component's dominance over the capacitive (reactive) component. However, the loss tangent falls, and the inverse trend becomes apparent as the frequency rises due to the independent nature of the ohmic part and the increasing reactive component with frequency. The resonance peak, which represents the highest energy transfer upon the application of a field, is likewise in good agreement with the Debye theoretical method [33].

3.4. Electrical conductivity

To better visualise, **Figure 8** shows the frequency dependence of conductance (σ) for different compositions of nZVI. The mentioned figure revealed that the conductivity of the various compositions is significantly high at low frequencies and low at high frequencies. This phenomenon is in line with the well-known Debye-Falkenhagen (DF) hypothesis, which states that the velocity of an ion is dynamically influenced by its ion environment. An external electric field cannot cause the atmosphere to follow the motion of the center ion when it moves in an electrolyte solution. This results in an asymmetrical effect that slows down the ion's speed. The center ion oscillates under an oscillating electric field, which also reduces the amount of time the ion atmosphere has to unwind and maintains its asymmetry. This results in an enhancement of the conductivity at low frequencies and a reduction of the relaxation force, which raises the rate of electron mobility. Due to the ions' rapid oscillation, which reduces the net ionic motion in a given direction when there is no static or low-frequency field present, conductivity drops at high frequencies [34].

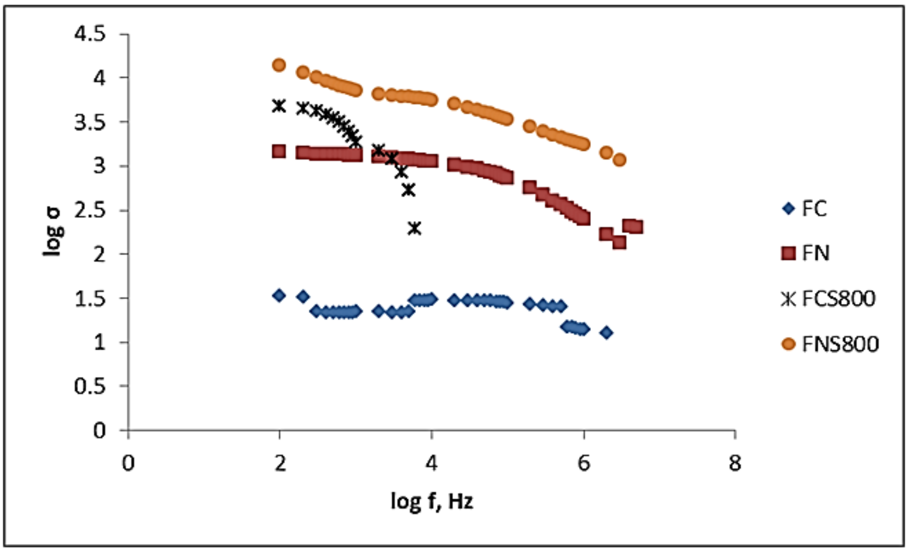

Figure 8. The variation of conductance (σ) of nZVI with frequency (*f*) for FC, FN, FCS800, and FNS800.

3.5. Alizarin removal via nZVI

3.5.1. Effect of contact time

One of the most important factors affecting the performance of adsorption processes for alizarin removal is the contact time between adsorbate and adsorbent. The effect of the contact time of FC and FN samples on the adsorption of alizarin red dye was investigated at pH 3 with a dosage of 0.01 g of adsorbent and an initial concentration of 150 mg/L. **Figure 9** illustrates the alizarin red dye adsorption capacities of synthesized adsorbents as a function of stirring times ranging between 10–240 min and 10–180 min for FC and FN, respectively. The rate of uptake was rapid at first and gradually increased in the later stages until it reached saturation, as shown in **Figure 9**. The maximum alizarin red dye removal was achieved in 180 and 120 min for FC and FN, respectively.

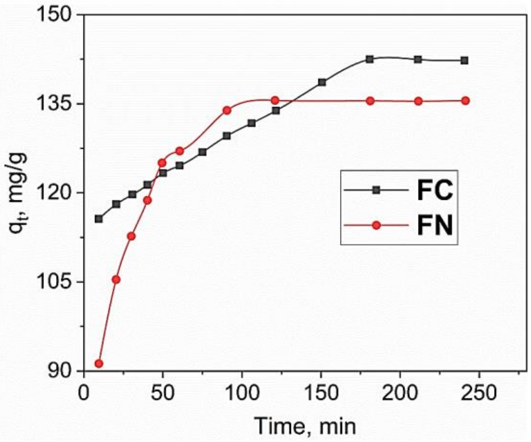

Figure 9. Effect of contact time on the adsorption capacities of FC and FN adsorbents for the removal of alizarin red dye.

3.5.2. Effect of initial dye concentration

The effect of varying the starting quantity of alizarin red dye from 50 to 350 mg/L on FC and FN was studied. These adsorption studies were carried out with a pH of 3 and a dosage of 0.01 g of adsorbent. The adsorbent was separated by centrifugation after 180 min for FC and 120 min for FN of stirring, and the residual dye concentration in the supernatant was determined using UV–Vis spectrophotometry. The rate of uptake was high at first and quickly approached saturation. As time passed, the active sites were blocked, and the rate fell, as indicated in **Figure 10** by the relationship between the adsorption capacity and the original dye concentration. From **Figure 10**, the adsorption capacities increased with increasing the initial concentration until they reached the maximum and constant high initial concentrations. From the data, the adsorption capacities of FC and FN samples were determined to be 139.029 and 99.416 mg/g, respectively.

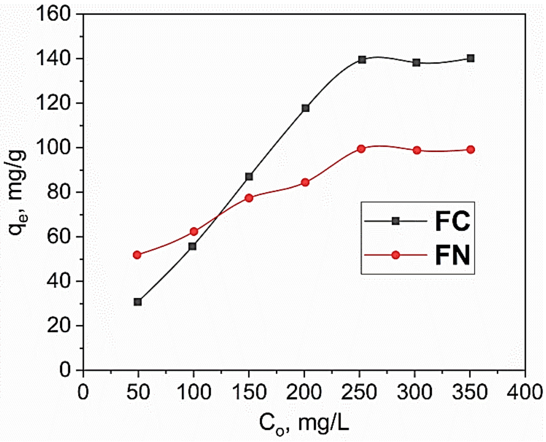

Figure 10. Effect of initial alizarin red dye concentration on adsorption capacities of FC and FN adsorbents for the removal of alizarin red dye.

3.5.3. Effect of adsorbent dose

One of the most important parameters that determines the adsorbent's capacity for a given initial adsorbate concentration is the adsorbent dosage. Using various doses of adsorbent (0.001–0.01 g), the effect of adsorbent dosage on the adsorption of alizarin red dye was investigated. At equilibrated time, the adsorbent was added to 50 mL of alizarin red dye solutions with initial concentrations of 150 mg/L for FC and FN. After the solutions had reached equilibrium, they were centrifuged and tested for dye content. The adsorption results are depicted in **Figure 11**. Because the adsorbent surface active size grows, the results suggest that increasing the adsorbent dosage increases dye removal efficiency. The maximum alizarin red dye removal percentages for FC and FN were found to be 92.786% and 85.206%, respectively, of the boundary layer enclosing the sorbent decreases. The adsorbate mass transfer resistance in the boundary layer decreased. This might have happened because, as the temperature increased, the dye's mobility increased (due to an increase in kinetic energy). The removal percentage of the alizarin red dye over the fabricated samples increased as the temperature of the dye solution decreased.

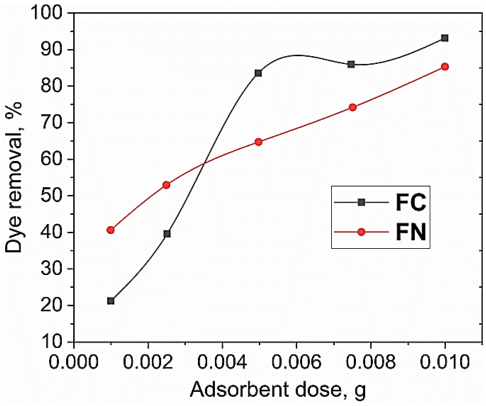

Figure 11. Effect of adsorbent dose on the alizarin red dye removal efficiency using FC and FN adsorbents.

4. Conclusion

nZVI were successfully prepared in the zero-oxidation state with 100% intensity at 2θ of 44.87° and 44.68° for FC and FN, respectively, with mean crystalline sizes of 3.166 and 1.83 nm, respectively, and there was no oxidation during storage for weeks through visual observation. SEM results showed that nZVI appear as spherical particles and take the shape of chain-like structures with a particle size in the range of 50–100 nm, and that nZVI have a strong trend to agglomerate in nanoscale aggregates due to the weak surface charges. The electrical properties of the various prepared nZVI compositions showed great variation with the use of different iron salt precursors. Further, the prepared nZVI obtained from iron chloride salt precursors were proven to be more capable adsorbents for alizarin red dye in aqueous solutions than those obtained from iron nitrate salt precursors. So, it is concluded that the type of salt precursor appears to have a high impact on the characteristic physical properties of the synthesized nanomaterial.

Author contributions: Completed the electrical conductivities of nZVI, IEH; wrote the article under consideration, IEH; explained the obtained results, IEH; proposed the idea of the present work, AAO; revised the present article, AAO; prepared the nZVI, described the structure via FE-SEM, and XRD, EEM. All authors have read and agreed to the published version of the manuscript.

Institutional review board statement: Not applicable.

Informed consent statement: Not applicable.

Conflict of interest: The authors declare no conflict of interest.

References

1. Galdames A, Ruiz-Rubio L, Orueta M, et al. Zero-Valent Iron Nanoparticles for Soil and Groundwater Remediation. Int. J. Environ. Res. Public Health. 2020; 17: 5817. doi:10.3390/ijerph17165817
2. Pasinszki T, Krebsz M. Synthesis and Application of Zero-Valent Iron Nanoparticles in Water Treatment, Environmental Remediation, Catalysis, and Their Biological Effects. Nanomaterials. 2020; 10: 917. doi: 10.3390/nano10050917
3. Pereira GM, Cellet TSP, Rubira AF, et al. Carbon-Capped Zerovalent Nickel and Cobalt Nanoparticles as Multitask Hybrid Electrocatalysts. ACS Appl. Energy. Mater. 2018; 1: 4939–4949. doi: 10.1021/acsaem.8b00955
4. Petrarca C, Poma AM, Vecchiotti G, et al. Cobalt magnetic nanoparticles as theranostics: Conceivable or forgettable? Nanotechnology Reviews. 2020; 9: 1522–1538. doi:10.1515/ntrev-2020-0111
5. Barka E, Noutsopoulos C, Galani A, et al. Removal of Contaminants of Emerging Concern from Wastewater Using an Integrated Column System Containing Zero Valent Iron Nanoparticles. Water. 2023; 15: 598. doi: 10.3390/w15030598
6. Qiao H, Han Y, Yao L, et al. Coating zero-valent iron onto hollow carbon spheres as efficient electrocatalyst for N2 fixation and neutral Zn-N2 battery. Chemical Engineering Journal. 2023; 464: 142628. doi: 10.1016/j.cej.2023.142628
7. Petrova E, Kotsikau D, Pankov V, et al. Influence of synthesis methods on structural and magnetic characteristics of Mg–Zn-ferrite nanopowders. Journal of Magnetism and Magnetic Materials. 2019; 473: 85–91. doi: 10.1016/j.jmmm.2018.09.128
8. Majid F, Shahin A, Ata S, et al. The effect of temperature on the structural, dielectric and magnetic properties of cobalt ferrites synthesized via hydrothermal method. Zeitschrift Für Physikalische Chemie. 2021; 235: 1279–1296. doi: 10.1515/zpch-2020-1751
9. Oropeza S, Corea M, Gómez-Yáñez C, et al. Zero-valent iron nanoparticles preparation. Materials Research Bulletin. 2012; 47: 1478–1485. doi: 10.1016/j.materresbull.2012.02.026
10. Torrey JD, Killgore JP, Bedford NM, et al. Oxidation behavior of zero-valent iron nanoparticles in mixed matrix water purification membranes. Environmental Science: Water Research & Technology. 2015; 1: 146–152. doi: 10.1039/C4EW00068D
11. Yuvakkumar R, Elango V, Rajendran V, et al. Preparation and characterization of zero-valent iron nanoparticles. Digest Journal of Nanomaterials and Biostructures. 2011; 6: 1771–1776.
12. Alymov MI, Rubtsov NM, Seplyarskii BS, et al. Preparation and characterization of iron nanoparticles protected by an oxide film. Inorg. Mater. 2017; 53: 911–915. doi: 10.1134/S0020168517090011
13. Yang R, Chen G, Laroche M, et al. Simulation of Nanoscale Multidimensional Transient Heat Conduction Problems Using Ballistic-Diffusive Equations and Phonon Boltzmann Equation. Journal of Heat Transfer. 2005; 127: 298–306. doi: 10.1115/1.1857941
14. Fujita K, Ando D, Uchikoshi M, et al. New model for low-temperature oxidation of copper single crystal. Applied Surface Science. 2013; 276: 347–358. doi: 10.1016/j.apsusc.2013.03.096
15. Lenglet M, Kartouni K, Machefert J, et al. Low temperature oxidation of copper: The formation of CuO. Materials Research Bulletin. 1995; 30: 393–403. doi: 10.1016/0025-5408(95)00025-9
16. Sarathy V, Tratnyek PG, Nurmi JT, et al. Aging of Iron Nanoparticles in Aqueous Solution: Effects on Structure and Reactivity. J. Phys. Chem. C. 2008; 112: 2286–2293. doi: 10.1021/jp0777418
17. Greenlee LF, Torrey JD, Amaro RL, et al. Kinetics of Zero Valent Iron Nanoparticle Oxidation in Oxygenated Water. Environ. Sci. Technol. 2012; 46: 12913–12920. doi: 10.1021/es303037k

18. Wang Y, Wang H, Chen H. Understanding role and mechanisms of zero-valent iron (ZVI) in activated sludge responses under glyphosate exposure. J. Water Proc. Eng. 2023; 55: 104210. doi: 10.1016/j.jwpe.2023.104210
19. Hu Y, Ke K, Sun H, et al. Coffee grounds modified zero-valent iron for efficient heavy metal removal. J. Water Proc. Eng. 2023; 56: 104397. doi: 10.1016/j.jwpe.2023.104397
20. Xu W, Huang D, Du L, et al. Recent advances on the incorporation of N into zero-valent and atomic iron for contaminants transformation. Coord. Chem. Rev. 2024; 505: 215671. doi: 10.1016/ j.ccr.2024.215671
21. Zhang F, Chen C, Zhou J, et al. Enhancing O2 resistance during storage and 2, 4-dichlorophenol degradation reaction of nano zero-valent iron by in-situ formation on the partially delignified stalk. Sep. Purif. Technol. 2024; 332: 125818. doi: 10.1016/j.seppur.2023.125818
22. Ding D, Zhao Y, Chen Y, et al. Recent advances in bimetallic nanoscale zero-valent iron composite for water decontamination: Synthesis, modification and mechanisms. J. Environ. Manag. 2024; 353: 120187. doi: 10.1016/j.jenvman.2024.120187
23. Fan M, Yuan P, Chen T, et al. Synthesis, characterization and size control of zerovalent iron nanoparticles anchored on montmorillonite. Chinese Science Bulletin. 2010; 55: 1092-1099. doi: 10.1007/s11434-010-0062-1
24. Jiemvarangkul P, Zhang W, Lien HL. Enhanced transport of polyelectrolyte stabilized nanoscale zero-valent iron (nZVI) in porous media. Chemical Engineering Journal. 2011; 170: 482–491. doi: 10.1016/j.cej.2011.02.065
25. Hwang Y, Kim D, Shin HS. Effects of synthesis conditions on the characteristics and reactivity of nano scale zero valent iron. Applied Catalysis B: Environmental. 2011; 105: 144-150.
26. Dutta S, Ghosh A, Satpathi S, et al. Modified synthesis of nanoscale zero-valent iron and its ultrasound-assisted reactivity study on a reactive dye and textile industry effluents. Desalination and Water Treatment, 2016; 57: 19321-19332. doi: 10.1080/19443994.2015.1096833
27. Khan MU, Jabeen N, Nawaz S, et al. Molarity Dependent Structural and Dielectric Behavior of Calcium Titanate Ceramics. American Journal of Engineering Research. 2021.
28. Tareev B, Tareev BM. Physics of Dielectric Materials, Mir Publ. MIR Publishing; 1979.
29. Mott NF. Conduction in glasses containing transition metal ions. Journal of Non-Crystalline Solids. 1968; 1: 1–17. doi: 10.1016/0022-3093(68)90002-1
30. Singh N, Agarwal A, Sanghi S. Dielectric relaxation, conductivity behaviour and magnetic properties of Mg substituted Ni–Li ferrites. Journal of Alloys and Compounds. 2011; 509: 7543–7548. doi: 10.1016/j.jallcom.2011.04.126
31. Prashant Kumar M, Sankarappa T, Vijaya Kumar B, et al. Dielectric relaxation studies in transition metal ions doped tellurite glasses. Solid State Sciences. 2009; 11: 214–218. doi: 10.1016/j.solidstatesciences.2008.05.015
32. Macedo PB, Moynihan CT, Bose R. Dielectric modulus: Experiment, application, and interpretation. J. Phy. Chem. Glasses. 1972; 13: 171.
33. Langar A, Sdiri N, Elhouichet H, et al. Conductivity and dielectric behavior of NaPO3–ZnO–V2O5 glasses. Journal of Alloys and Compounds. 2014; 590: 380–387. doi: 10.1016/j.jallcom.2013.12.130
34. Bahgat AA. Study of dielectric relaxation in Na-doped Bi–Pb–Sr–Ca–Cu–O glasses. Journal of Non-Crystalline Solids. 1998; 226: 155–161. doi: 10.1016/S0022-3093(97)00482-1